[redacted]

[redacted]

Copy
RM L54D29

TECH LIBRARY KAFB, NM
0144237

NACA RM L54D29

7544

NACA

RESEARCH MEMORANDUM

LOW-AMPLITUDE DAMPING-IN-PITCH CHARACTERISTICS OF TAILLESS DELTA-WING—BODY COMBINATIONS AT MACH NUMBERS FROM 0.80 TO 1.35 AS OBTAINED WITH ROCKET-POWERED MODELS

By Charles T. D'Aiutolo

Langley Aeronautical Laboratory
Langley Field, Va.

[redacted]

[redacted]

NATIONAL ADVISORY COMMITTEE
FOR AERONAUTICS
WASHINGTON
June 24, 1954

[redacted]

[redacted]

~~CONFIDENTIAL~~

TECH LIBRARY KAFB, NM

0144237

NATIONAL ADVISORY COMMITTEE FOR AERONAUTICS

RESEARCH MEMORANDUM

LOW-AMPLITUDE DAMPING-IN-PITCH CHARACTERISTICS OF TAILLESS DELTA-WING—BODY COMBINATIONS AT MACH NUMBERS FROM 0.80 TO 1.35 AS OBTAINED WITH ROCKET-POWERED MODELS

By Charles T. D'Aiutolo

SUMMARY

A free-flight investigation was conducted using three rocket-propelled delta-wing—body combinations between the Mach numbers of 0.80 and 1.35. The configurations tested were an aspect-ratio-2 delta-wing—body combination with afterbody, an aspect-ratio-2 delta-wing—body combination with no afterbody, and an aspect-ratio-3 delta-wing—body combination with afterbody. All models incorporated NACA 63A006 airfoil sections parallel to the free stream.

The results indicated that all models were statically stable but were dynamically unstable, to various degrees, at transonic speeds. The damping was extremely low at subsonic and supersonic speeds, and a decrease of aspect ratio decreased the Mach number range over which dynamic instability occurred.

An application of the effect of dynamic instability on the performance of a full-scale airplane has been made from the data obtained from the flight-test results.

INTRODUCTION

Since flight speeds have progressed into the transonic and low supersonic speed ranges, the need for the determination of the dynamic longitudinal stability characteristics of aircraft configurations traversing these speed regions has become paramount. These characteristics are especially desired for the tailless delta-wing configuration since theoretical calculations (ref. 1) indicate that the dynamic longitudinal stability of these designs is low and that for some Mach numbers and center-of-gravity positions dynamic instability will exist. Therefore,

~~CONFIDENTIAL~~

an experimental study of the effects of various parameters on the dynamic stability of tailless delta airplane configurations is desired.

Recently the results of systematic studies of the effects of some parameters on the damping-in-pitch characteristics of tailless delta airplane configurations at subsonic and supersonic speeds were published. (See refs. 2 and 3.) It was impossible in these investigations to obtain results in the transonic speed range because of the limitations of the test facilities. A desire, therefore, exists for the determination of these data in the transonic speed range.

It is the purpose of this report to determine experimentally the regions of dynamic instability at transonic speeds and low supersonic speeds and to determine the effects of aspect ratio on this dynamic instability.

This report is a continuation of the investigation reported in reference 4 and contains the results from the flight tests, conducted by the Pilotless Aircraft Research Division, of an aspect-ratio-2 delta-wing—body combination with afterbody, an aspect-ratio-2 delta-wing—body combination with no afterbody, and an aspect-ratio-3 delta-wing—body combination with afterbody. All wings had NACA 63A006 airfoil sections parallel to the free stream. The data are presented over a Mach number range of about 0.80 to 1.35 corresponding to a Reynolds number range of about 9×10^6 to 20×10^6, respectively.

The static and dynamic longitudinal stability characteristics of the models were determined by analyzing the oscillations produced in pitch by firing small rocket motors which were mounted to provide thrust normal to the longitudinal axis of the models. The drag characteristics were determined from the deceleration of the models as they coasted through the speed range. The models were flown at the Langley Pilotless Aircraft Research Station, Wallops Island, Va.

SYMBOLS

V	velocity of flight, ft/sec
M	Mach number, $\frac{V}{\text{Speed of sound}}$
S	total wing area, sq ft
$\bar{c}$	mean aerodynamic chord, ft

A	aspect ratio
A'	cross-sectional area of any longitudinal station, sq ft
l	body length, ft
X	distance along body measured from nose, ft
ρ	air density, slugs/cu ft
R	Reynolds number (based on mean aerodynamic chord of respective models)
q	dynamic pressure, lb/sq ft
b	total damping factor (logarithmic decrement of pitch oscillation), radians/sec
$T_{1/2}$	time required for short-period oscillation to damp to one-half amplitude, sec
T_2	time required for short-period oscillation to double amplitude, sec
k	reduced-frequency parameter (based on respective mean aerodynamic chord of models), $\frac{\omega \bar{c}}{2V}$
$\bar{X}_{a.c.}$	distance from leading edge of mean aerodynamic chord to aerodynamic center of model, percent of mean aerodynamic chord, positive rearward
C_L	lift coefficient, Lift/qS
C_{L_α}	slope of lift curve, per degree
C_m	pitching-moment coefficient, $\frac{\text{Moment}}{qS\bar{c}}$
C_{m_α}	static stability derivative, per degree

$C_{m_q} = \dfrac{\partial C_m'}{\partial \frac{\dot{\theta}\bar{c}}{2V}}$, per radian

$C_{m_{\dot{\alpha}}} = \frac{\partial C_m}{\partial \frac{\dot{\alpha}\bar{c}}{2V}}$, per radian

C_D drag coefficient

α angle of attack, measured from fuselage reference line, deg

$\dot{\alpha} = \frac{1}{57.3}\frac{d\alpha}{dt}$, radian/sec

θ angle of pitch, measured from fuselage reference line, radians

$\dot{\theta} = \frac{d\theta}{dt}$, radians/sec

t time, sec

ω frequency of short-period oscillation, radians/sec

$\mu = \frac{m}{\rho S\bar{c}}$ relative-density factor

MODELS AND APPARTUS

The general arrangements of the models are shown in figure 1, and the geometric characteristics of the models are presented in table I. A photograph of one of the models is presented in figure 2, and a photograph of one of the models on the rocket launcher is shown in figure 3. The cross-sectional-area distribution of each of the models is presented in figure 4, for possible correlation of drag results.

Each model consisted of a basic fuselage to which was attached the wing under test. The fuselage was a body of revolution, consisting of an ogival nose section and a cylindrical body section. Construction of the fuselage was of duralumin with magnesium skin. The nose section contained the telemeter and the cylindrical body section contained the wing mount, necessary fairings, the vertical tails, and, for models 1 and 3, the sustainer rocket motor. The fuselage of model 2 terminated at the trailing edge of the wing so that there was no afterbody and the cylindrical body section did not contain a sustainer rocket motor.

The wings of the models were constructed of wood with sheet aluminum inlays (for structural purposes) and were mounted on the fuselage (as shown in fig. 1) with the resultant center of gravity at 17 percent of the mean aerodynamic chord.

All models contained a four-channel telemeter. Measurements were made of the normal and longitudinal accelerations, angle of attack (measured by a vane-type instrument located on a sting forward of the nose of the models (see ref. 5)), and total pressure (measured by a tube located on a strut below the fuselage of the models).

Velocity data were obtained by CW Doppler radar; range and elevation of the models during flight, by tracking radar; atmospheric conditions, by radiosonde. The first portion of the flights was recorded by special cameras.

Models 1 and 3 contained a cordite sustainer rocket motor and were boosted by a light-weight 5-inch HVAR rocket motor. Upon burnout of the booster rocket motor, the model separated from the booster, the sustainer rocket motor fired, and the model was propelled to its maximum speed. Upon burnout of the sustainer rocket motor, the model coasted throughout the test speed range. Model 2, which did not contain a sustainer rocket motor, was boosted to its maximum speed by an ABL Deacon rocket motor. Upon burnout of the booster rocket motor, the model separated from the booster and coasted throughout the speed range.

Models 1 and 2 together with their boosters were launched from a rail-type launcher as shown in figure 3. Model 2 and its booster were launched from a mobile zero-length type of launcher.

All model-booster combinations were launched at an angle of approximately 45°.

TEST AND ANALYSIS

Test

The data for each model were obtained during the decelerating part of the flights, that is, after sustainer motor burnout. It was intended to disturb each model in pitch by a series of small rocket motors providing thrust normal to the longitudinal axis of the model and located near the rear of the model. These rocket motors were designed to fire during the decelerating portion of the flights so that the data could be obtained over a Mach number range during the coasting phase of the flights. The firing sequence of these small rocket motors was such that the oscillation caused by the firing of one of the small rocket motors would damp to an approximate trim angle of attack before the next small rocket motor was fired. Model 1 contained four of these small rocket motors and all of them fired, but the first one fired during the latter part of sustainer motor burning. Because of an electrical failure, all eight small rocket motors contained in model 2 failed so that model 2 was not disturbed in pitch as the model traversed the Mach number range. Model 3 contained four pulse rockets and three of the four fired; however, the first small rocket fired during the latter part of sustainer motor burning.

Time histories of angle of attack, lift coefficient, and Mach number covering the decelerating portions of the flights and the times at which the small pulse rocket motors were fired for each of the three models are shown in figure 5. Also shown are the envelopes drawn for each oscillation in pitch that were caused by the firing of the small pulse rockets. The desired static and dynamic longitudinal stability derivatives were obtained from these oscillations. However, it was only possible to determine these derivatives for models 1 and 3 since the small rocket motors contained in model 2 failed to fire and the oscillations experienced by model 2 as it traversed the speed range were not free oscillations but forced oscillations of a random nature.

Roll data, obtained from spinsonde records, indicated that for the three models the rate of roll was approximately zero.

Figures 6, 7, and 8 present, respectively, the variation of air density, velocity, and dynamic pressure with Mach number for each of the tests. These quantities are presented so that a possible correlation of the data obtained from these tests with data obtained from other tests may be made.

The scale of the tests is presented in figure 9 where Reynolds number is plotted against Mach number (the Reynolds number is based on the respective mean aerodynamic chords).

Accuracy

It is impossible to determine exactly the limits of accuracy of each quantity derived from these free-flight model tests. In general, however, the absolute value of any telemetered measurement can be in error by 2 to 5 percent of the calibrated instrument range. The Doppler radar velocity is known to be accurate to better than 2 percent. Since Mach number was determined from Doppler radar velocity, it should be accurate to 2 percent. The derivative C_{L_α} and the coefficient C_D are subject to error because they depend upon the measured normal and longitudinal accelerations and angle of attack, as well as the dynamic pressure. Since C_{m_α} is determined essentially from the period of the oscillation, it will be unaffected by the error in the measured values of the angle of attack or normal acceleration but will be affected by the errors in dynamic pressure and the determination of the moment of inertia. The aerodynamic-center location should be unaffected by errors in dynamic pressure because it depends upon the ratio $C_{m_\alpha}/C_{L_\alpha}$.

The total damping factor b should be affected by errors in the measured quantities of angle of attack and normal and longitudinal accelerations, as well as errors in fairing the envelopes of the oscillations and errors in determining slopes, and is considerably more inaccurate than the other derivatives. The errors in the total damping factor are reflected directly into the damping-in-pitch derivatives $C_{m_q} + C_{m_{\dot{\alpha}}}$.

Analysis

After the firing of each pulse rocket the models experienced short-period oscillations in pitch as shown in figure 5. These oscillations were analyzed to obtain the static and dynamic longitudinal stability characteristics of each of the models. The method of analysis used to reduce all the data except the total damping factor b is described in detail in appendix A of reference 6. Since it was felt that the total damping factor b of the models would be changing rapidly throughout the transonic speed range, the method described in reference 6 to determine the total damping factor b was not used, but the following procedure was employed:

(1) The envelopes of the oscillations in angle of attack and lift coefficient were drawn and trim values of these quantities were obtained from the midpoint between the envelopes (see fig. 5).

(2) The amplitudes of the oscillations were obtained (value measured from the trim to the envelope). These amplitudes were then plotted on Cartesian coordinate graph paper and a curve defining the relation between the oscillation amplitude and time was determined.

(3) This relationship was then plotted on semilog graph paper with the oscillation amplitude plotted along the log scale and a curve faired through the points.

(4) From this semilog plot, the time for the oscillation to damp to one-half amplitude or the time for the oscillation to double amplitude was determined. When the variation of the oscillation amplitude with time, when plotted on semilog graph paper, was a straight line one value of $T_{1/2}$ or T_2 was obtained for the complete oscillation. However, when the variation was a curve, values of $T_{1/2}$ or T_2 were obtained

over arbitrarily selected values of time. The results were plotted against the Mach number corresponding to these times.

(5) From the time to damp to one-half amplitude, the total damping factor b was obtained from the following expression

$$b = -\frac{0.693}{T_{1/2}}$$

While from the time to double amplitude, the total damping factor b was obtained from the following expression

$$b = \frac{0.693}{T_2}$$

Order of Oscillation Frequency

From the periods of the short-period oscillations of each model, the reduced-frequency parameter $k = \frac{\omega\bar{c}}{2V}$ (based on respective mean aerodynamic chords) was determined. Inasmuch as the values of k that were determined were less than 0.036, it is believed that second-order frequency effects are not important in the determination of the damping-in-pitch derivatives and that the method of reducing the data presented in the "Analysis" section gives good results for these derivatives.

RESULTS AND DISCUSSION

The stability parameters of the models presented in this paper were determined from the coasting phase of the flights. All the models were tested with the center of gravity located at 17 percent of the mean aerodynamic chord behind the leading edge of the mean aerodynamic chord.

Trim

The trim characteristics of each model are shown in figure 5. Note that the ordinates of figure 5(b) are plotted to a larger scale than the ordinates of figures 5(a) and 5(c). Model 1 flew at a trim angle of attack of approximately -1.0° throughout the flight corresponding to a zero-lift condition and did not experience a trim change in the transonic speed range. Model 2 flew at a trim angle of attack of approximately -0.15°

at high subsonic speeds corresponding to a lift coefficient of approximately -0.015 and experienced a nose-up trim change at transonic speeds. At supersonic speeds, model 2 flew at an angle of attack of approximately 0° corresponding to an approximate zero-lift condition. Model 3 flew at an approximate angle of attack of -0.5° corresponding to a zero-lift condition throughout the flight and did not experience a trim change in the transonic speed range.

Lift

The variation of the slope of the lift curve C_{L_α} with Mach number is presented in figure 10. These data are presented for models 1 and 3 only since, as previously mentioned, the small rocket motors contained in model 2 failed to fire and the forced oscillations in angle of attack experienced by model 2 were not used to determine C_{L_α}.

By comparing the lift-curve slopes of models 1 and 3, as shown in figure 10, it may be seen that at transonic and supersonic speeds, the values of C_{L_α} for model 1 ($A = 2$) and model 3 ($A = 3$) were closer than expected. This variation disagrees with the predicted variation when considering the difference in aspect ratio. The values of C_{L_α} for model 3 ($A = 3$) should be considerably higher than the values of C_{L_α} for model 1 ($A = 2$) throughout the speed range provided, of course, that both models were identical in stiffness (i.e., identical degree of flexibility). During preflight checks it was found that the wings of model 1 were more rigidly attached to the fuselage than were the wings of model 3; therefore, model 3 was more flexible than model 1 and would be more susceptible to aeroelastic effects.

To determine the degree of this flexibility, static twist tests were performed on the wings of models 1 and 3 while attached to the fuselages (see appendix of ref. 7). On the basis of these tests, the values of C_{L_α} for model 1 should be identical to rigid-wing values at subsonic and supersonic speeds, and the values of C_{L_α} for model 3 should be reduced 20 percent at subsonic speeds and 30 percent at supersonic speeds from rigid-wing values.

These static twist data are substantiated in figure 10 where the C_{L_α} value of models 1 and 3 is compared with wind-tunnel values of C_{L_α} (ref. 8). The wind-tunnel models were constructed basically of steel and are considered rigid. The data of model 1 agree with the wind-tunnel data throughout the speed range, while the values of C_{L_α} for model 3 are about 17 percent lower at subsonic speeds and about 32 percent lower at supersonic speeds than the wind-tunnel values of C_{L_α}. Note that the differences in the values of C_{L_α} as obtained for model 3 and the wind-tunnel tests become greater as the dynamic pressure becomes greater, further indicating that model 3 was quite flexible. This effect was not apparent for model 1.

Static Longitudinal Stability

The static longitudinal stability for model 1 $(A = 2)$ and model 3 $(A = 3)$ is presented in figures 11 and 12 where the variations with Mach number of the slope of the pitching-moment curve and the aerodynamic-center location are shown, respectively. Figure 11 shows that, for both models, the values of C_{m_α} increase with increasing Mach number through the transonic speed range, then decrease somewhat as the Mach number became greater than one. The data of figure 12 indicate an abrupt increase in static stability in the transonic speed range and a gradual decrease at supersonic speeds.

Dynamic Longitudinal Stability

Total damping factor.- From the time history of the pitch oscillations encountered during the flights of the models (see fig. 5), the total damping factor b was obtained. This total damping factor b includes the contributions of moment due to motion along a curved path at constant angle of attack C_{m_q}, the moment due to plunging motion with constant vertical acceleration $C_{m_{\dot{\alpha}}}$, and the translation effect of C_{L_α}. The variation of b with Mach number for models 1 and 3 is presented in figure 13. By use of the method presented in the "Analysis" section, it was possible to determine numerous instantaneous values of b near $M = 1.0$ and at high subsonic speeds such that the curves that appear in figure 13 represent values that were determined from experimental test data points only. At low supersonic speeds, the curves represent fairings through data that were obtained at two supersonic Mach numbers. Superimposed on these curves near $M = 1.0$ are broken vertical lines which indicate regions where limited data were determined from the tests. For model 1 $(A = 2)$, this region represents data that were determined from a limited number of cycles. By referring to figure 5(a), it may be seen that near $M = 1.0$ the envelopes of the oscillations were determined from about three cycles so that the envelopes could not be very well defined because of the rapid changes in damping. For model 3 $(A = 3)$, the region represents data that were determined from angle-of-attack oscillations that were less than 0.1° in amplitude. (See fig. 5(c) near $M = 0.9$.) These oscillations were considerably more regular than those of model 2 (see fig. 5(b)) and only occurred in the region near $M = 0.9$.

Figure 13 shows that for each model there is an abrupt decrease in the total damping factor from negative (stable) to positive (unstable) values for relatively small increments of Mach number at transonic speeds. As the Mach number further increases, the total damping factor increases and becomes stable for both models. It may be noted that model 3 ($A = 3$) experienced dynamic instability at a lower Mach number than model 1 ($A = 2$); also, this dynamic instability existed over a wider region of Mach number than for model 1.

The two data points near $M = 0.9$ for model 1 ($A = 2$) were determined from an oscillation whose envelopes when plotted on semilog graph paper had two distinct slopes. This characteristic was not apparent in any of the other oscillations, nor was it apparent in any of the oscillations experienced by model 3 ($A = 3$). The higher value of the total damping factor, $b = -3.90$, was obtained from an oscillation-amplitude range of $0.25^\circ \leqq \alpha \leqq 1.00^\circ$, while the lower value of the total damping factor, $b = -2.40$, was obtained from an oscillation amplitude range of $1.00^\circ \leqq \alpha \leqq 1.50^\circ$. Since the Mach number as well as the oscillation amplitude was different for each of these slopes, the curves showing the trend of b with Mach number were not faired through these points since it was not known whether the difference in b is due to Mach number or oscillation amplitude or both.

Although these oscillations showed that the models had low dynamic stability, the motions were not violent and the models traversed the speed range with no adverse effects. (See fig. 5.)

Rotational damping-in-pitch derivatives.- The total damping factor b as obtained for models 1 and 3 was reduced to determine the rotational damping-in-pitch derivatives $C_{m_q} + C_{m_{\dot{\alpha}}}$ on the basis of steady flows. These data are presented in figure 14 where the effect of aspect ratio on $C_{m_q} + C_{m_{\dot{\alpha}}}$ is indicated.

At transonic speeds, the data for model 1 ($A = 2$) and model 3 ($A = 3$) show the same variation in that there is an abrupt decrease in $C_{m_q} + C_{m_{\dot{\alpha}}}$ over a small transonic Mach number range; however, $C_{m_q} + C_{m_{\dot{\alpha}}}$ for model 3 ($A = 3$) becomes unstable at a lower transonic Mach number than $C_{m_q} + C_{m_{\dot{\alpha}}}$ for model 1 ($A = 2$). At supersonic speeds, $C_{m_q} + C_{m_{\dot{\alpha}}}$ for model 1 ($A = 2$) becomes stable at $M = 1.02$, while $C_{m_q} + C_{m_{\dot{\alpha}}}$ for model 3 ($A = 3$) becomes stable at $M = 1.07$. Note that the Mach number range over which instability exists is extremely small for model 1 ($A = 2$). Also the Mach number range over which instability occurs decreases with decreasing aspect ratio. The results of reference 4 indicate that, for an $A = 4$ delta-wing—body combination, dynamic instability occurs over a wider range of Mach number than for either the $A = 2$ or $A = 3$ configurations.

The two test points near $M = 0.90$ indicate values of $C_{m_q} + C_{m_{\dot{\alpha}}}$ that were determined from the data of figure 13 at the corresponding Mach numbers.

Also presented in figure 14 are the theoretical supersonic Mach numbers below which dynamic instability will occur as predicted by the theory of reference 9. The theory predicted that, for a center-of-gravity position located at 17 percent of the mean aerodynamic chord, dynamic instability would occur below $M = 1.007$ for the $A = 2$ configuration and below $M = 1.054$ for $A = 3$ configuration. Comparing these Mach numbers with the corresponding experimental Mach numbers indicates that the theory of reference 9 is reliable in predicting the Mach number below which dynamic instability exists at supersonic speeds.

For the $A = 2$ configuration the rapidly changing $C_{m_q} + C_{m_{\dot{\alpha}}}$ near $M = 1$ from negative (stable) to positive (unstable) and finally to negative (stable) values can be seen in figure 5(a) where near $M = 1$ the envelopes of the oscillation in angle of attack and lift coefficient converge then diverge and finally converge.

The test data of figure 14 were applied to a hypothetical full-scale airplane to determine the conditions of flight at which dynamic instability would occur. By assuming that the relative density factors of the models and the full-scale airplane were identical, it was found that the full-scale airplane would experience dynamic instability over the same Mach number range as the models reported in this paper but at an altitude of approximately 50,000 feet. Inasmuch as this altitude can be attained by present-day aircraft, an attempt will be made to determine how this dynamic instability will affect the performance of the airplane.

By referring to figure 5 (particularly fig. 5(b)), it can be seen that the motions experienced are not violent and that the airplane would traverse the speed range with no difficulty provided that the performance of the airplane is not limited to transonic speeds less than $M = 1.3$. However, if the performance is limited to transonic speeds at an altitude of 50,000 feet, this dynamic instability (see fig. 5) would present a problem. As the region of dynamic instability is approached, the oscillations in pitch would increase in amplitude and the total drag of the airplane would increase abruptly because of the drag due to lift. As a result, the speed of the airplane will decrease rapidly and the airplane will be flying below the speed region for dynamic instability. Therefore, the problem of dynamic instability that the full-scale airplane would experience at an altitude of 50,000 feet and at transonic speeds is not a severe one in that the results are not catastrophic, but it is a problem in performance which in many cases may severely restrict the mission that the airplane is required to fulfill.

Drag

The variation of the drag coefficient with Mach number for the three models is presented in figure 15. The effect of the afterbody on the drag may be seen by comparing models 1 and 2. Models 1 and 2 experienced about the same peak drag coefficient, but at supersonic speeds the drag coefficient of model 1 is lower than that for model 2. The trend of these results agrees with the results of reference 10. The drag rise of model 3 is lower than that of models 1 and 2.

CONCLUSIONS

From the results of the free-flight tests of three delta-wing—body combinations - an aspect-ratio-2 delta-wing—body combination with afterbody, an aspect-ratio-2 delta-wing—body combination with no afterbody, and an aspect-ratio-3 delta-wing—body combination with afterbody, all incorporating NACA 63A006 airfoil sections - the following conclusions may be stated:

1. All models were statically stable throughout the Mach number range investigated ($M = 0.80$ to 1.35) but were dynamically unstable, to various degrees, at transonic speeds.

2. The total damping factor as well as the rotational damping-in-pitch derivatives were extremely small at subsonic and supersonic speeds and were unstable at transonic speeds.

3. The effects of decreasing the aspect ratio were to decrease the Mach number range over which dynamic instability occurs. Also the theory predicted the trend with aspect ratio of the supersonic Mach number at which zero damping occurred.

4. The data of the free-flight tests when applied to a full-scale airplane indicated that although the dynamic instability would present a problem in the performance of the airplane, the overall results would not be catastrophic.

Langley Aeronautical Laboratory,
National Advisory Committee for Aeronautics,
Langley Field, Va., April 29, 1954.

REFERENCES

X 1. Ribner, Herbert S., and Malvestuto, Frank S., Jr.: Stability Derivatives of Triangular Wings at Supersonic Speeds. NACA Rep. 908, 1948. (Supersedes NACA TN 1572.)

2. Tobak, Murray: Damping in Pitch of Low-Aspect-Ratio Wings at Subsonic and Supersonic Speeds. NACA RM A52L04a, 1953.

3. Beam, Benjamin H.: The Effects of Oscillation Amplitude and Frequency on the Experimental Damping in Pitch of a Triangular Wing Having an Aspect Ratio of 4. NACA RM A52G07, 1952.

4. D'Aiutolo, Charles T., and Parker, Robert N.: Preliminary Investigation of the Low-Amplitude Damping in Pitch of Tailless Delta- and Swept-Wing Configurations at Mach Numbers From 0.7 to 1.35. NACA RM L52G09, 1952.

5. Mitchell, Jesse L., and Peck, Robert F.: An NACA Vane-Type Angle-of-Attack Indicator for Use at Subsonic and Supersonic Speeds. NACA RM L9F28a, 1949.

6. Gillis, Clarence L., Peck, Robert F., and Vitale, A. James: Preliminary Results From a Free-Flight Investigation at Transonic and Supersonic Speeds of the Longitudinal Stability and Control Characteristics of an Airplane Configuration With a Thin Straight Wing of Aspect Ratio 3. NACA RM L9K25a, 1950.

7. Vitale, A. James: Effects of Wing Elasticity on the Aerodynamic Characteristics of an Airplane Configuration Having 45° Sweepback Wings As Obtained From Free-Flight Rocket-Model Tests at Transonic Speeds. NACA RM L52L30, 1953.

X 8. Hall, Charles F.: Lift, Drag, and Pitching Moment of Low-Aspect-Ratio Wings at Subsonic and Supersonic Speeds. NACA RM A53A30, 1953.

X 9. Watkins, Charles E., and Berman, Julian H.: Air Forces and Moments on Triangular and Related Wings With Subsonic Leading Edges Oscillating in Supersonic Potential Flow. NACA Rep. 1099, 1952.

10. Love, Eugene S.: The Base Pressure at Supersonic Speeds on Two-Dimensional Airfoils and Bodies of Revolution (With and Without Fins) Having Turbulent Boundary Layers. NACA RM L53C02, 1953.

TABLE I.- GEOMETRIC CHARACTERISTICS OF THE MODELS

	Model 1	Model 2	Model 3
Wing:			
Total area, sq ft	5.00	5.00	5.00
Span, ft	3.16	3.16	3.87
Aspect ratio	2	2	3
Mean aerodynamic chord, ft	2.11	2.11	1.72
Sweepback of leading edge	63° 26'	63° 26'	53° 04'
Dihedral, deg	0	0	0
Taper ratio	0	0	0
NACA airfoil sections parallel to free stream	63A006	63A006	63A006
Fuselage:			
Length, in.	75.00	57.80	75.00
Fineness ratio	10.70	8.26	10.70
Miscellaneous:			
Model weight, lb	113.5	135.5	115.5
Moment of inertia in pitch, I_Y, slug-ft^2	11.20	14.06	11.00
Center-of-gravity position, percent M.A.C.	17	17	17
Wing loading, lb/sq ft	22.7	27.1	23.1
Relative-density factor, μ			
At $M = 0.80$	173	220	204
At $M = 1.25$	158	190	178

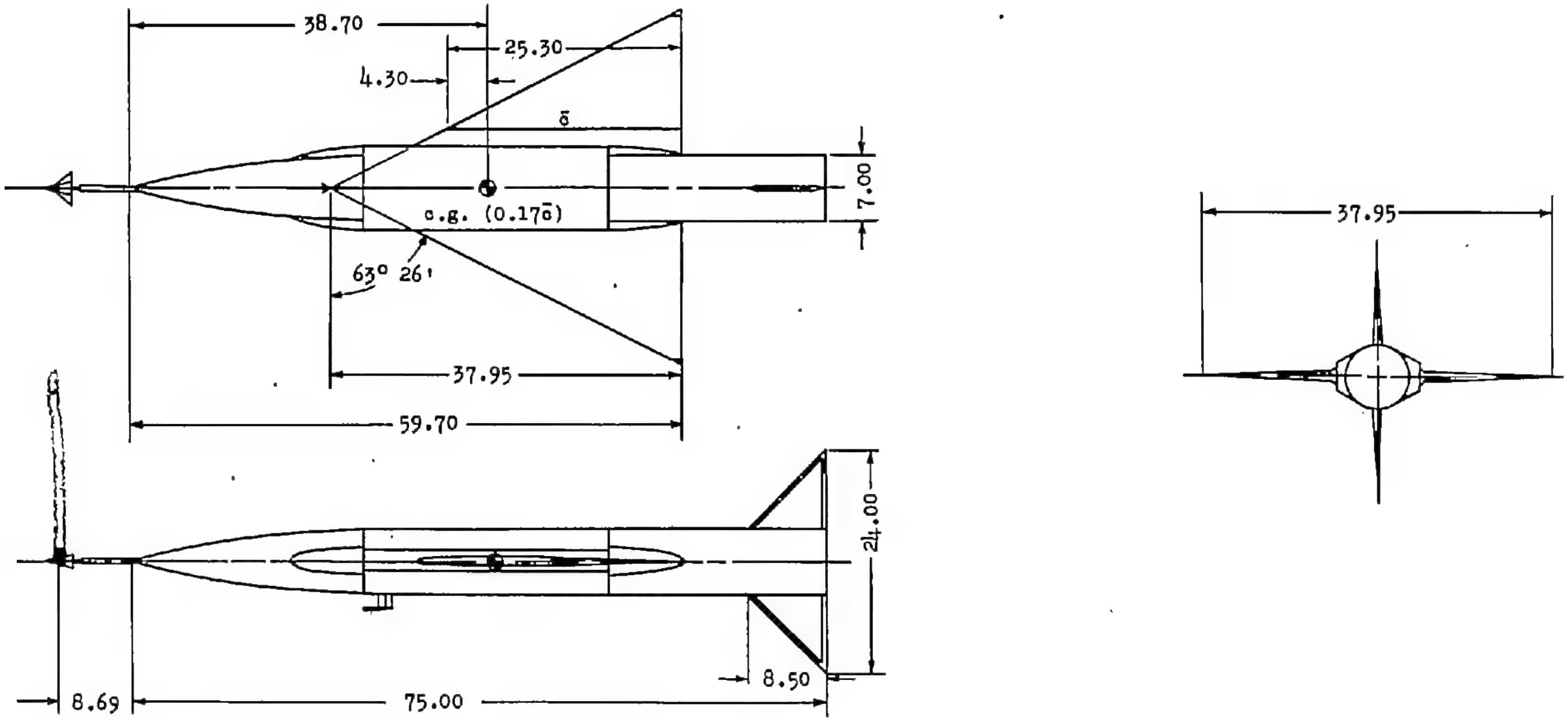
38.70
25.30
4.30
c̄
7.00
c.g. (0.17c̄)
63° 26'
37.95
59.70
24.00
8.50
8.69
75.00
37.95

(a) Model 1. With afterbody; A = 2.

Figure 1.- General arrangement of models. Airfoil sections, NACA 63A006; all dimensions in inches unless otherwise noted.

~~CONFIDENTIAL~~

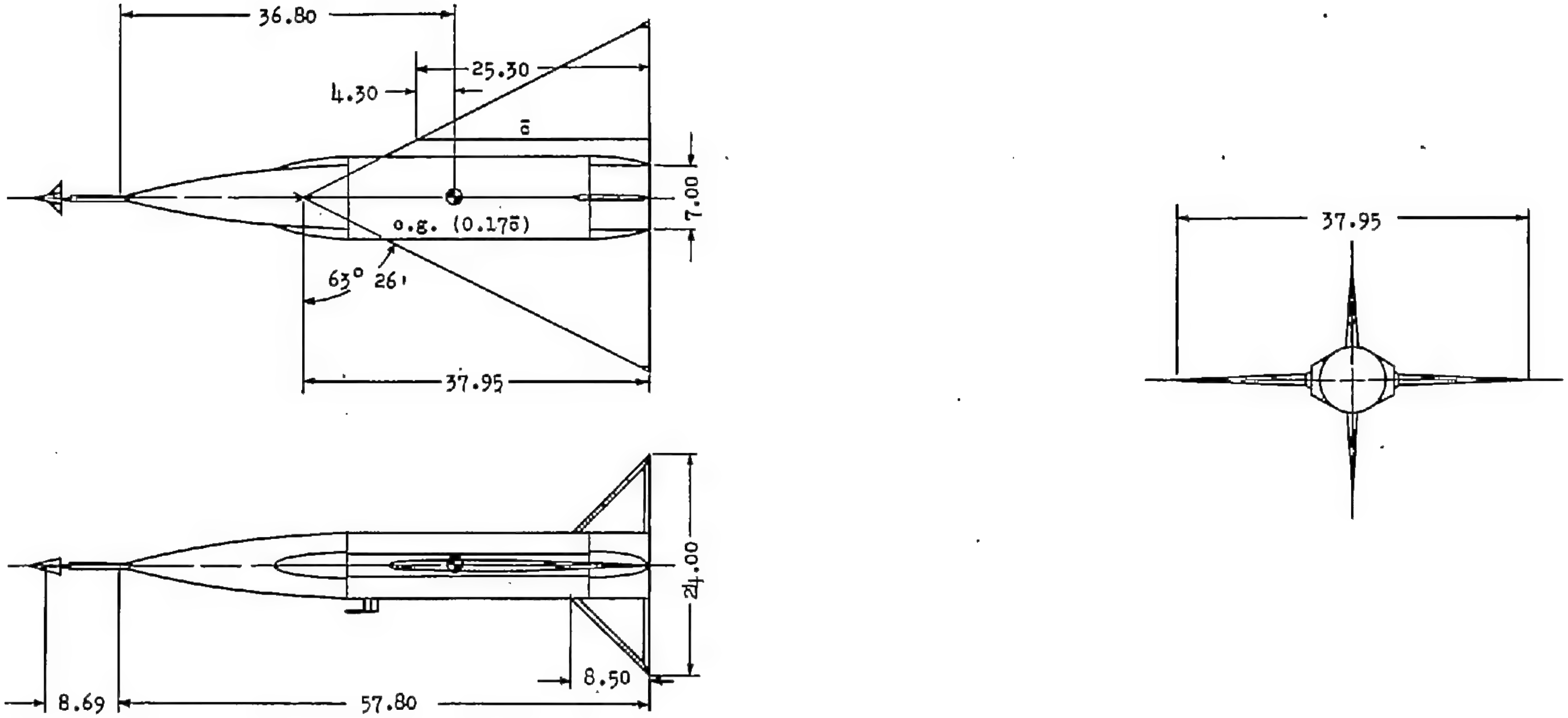
36.80
25.30
4.30
c̄
7.00
c.g. (0.17c̄)
63° 26'
37.95
24.00
8.50
8.69
57.80
37.95

(b) Model 2. No afterbody; A = 2.

Figure 1.- Continued.

~~CONFIDENTIAL~~

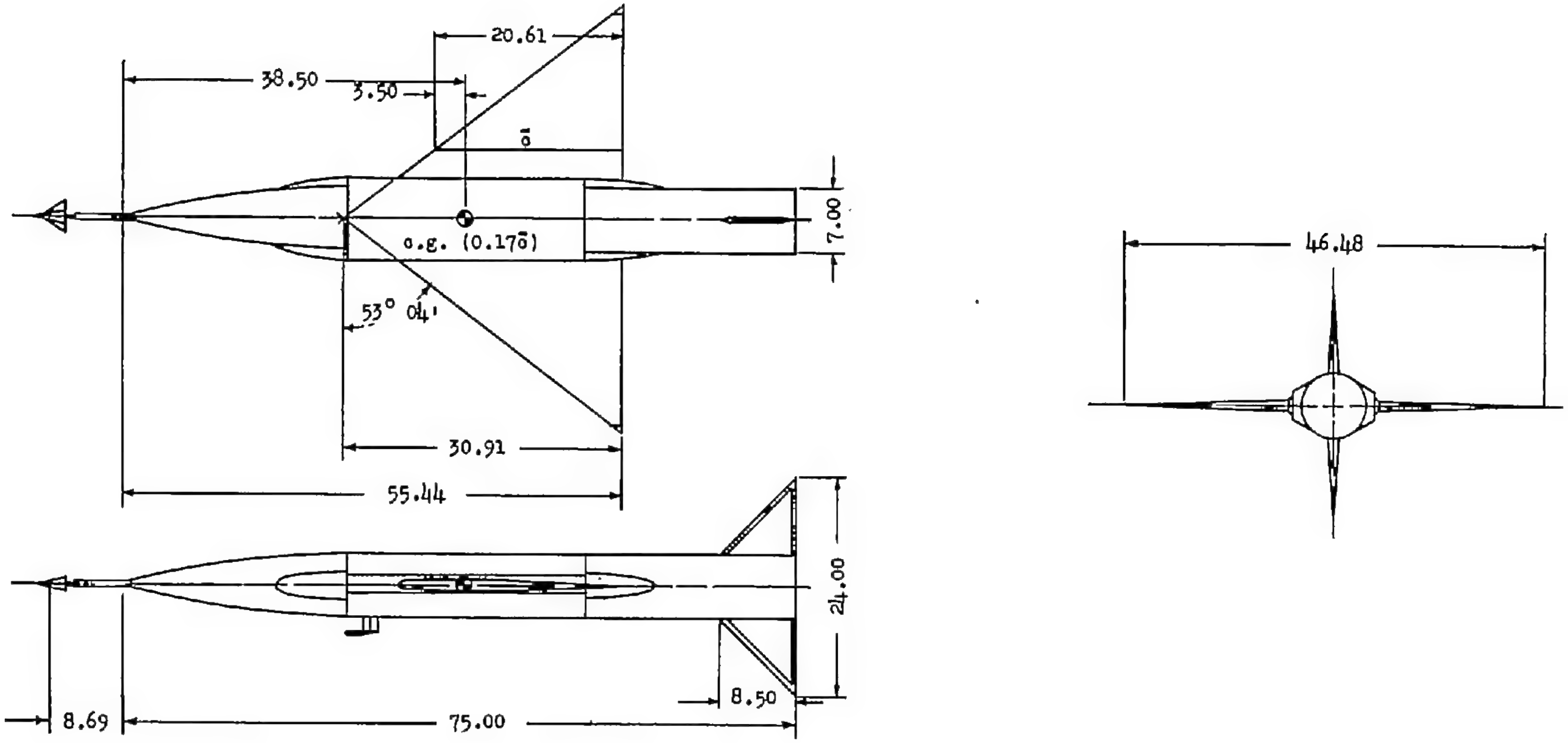
20.61
38.50
3.50
c̄
7.00
c.g. (0.17c̄)
53° 04'
30.91
55.44
24.00
8.50
8.69
75.00
46.48

(c) Model 3. With afterbody; A = 3.

Figure 1.- Concluded.

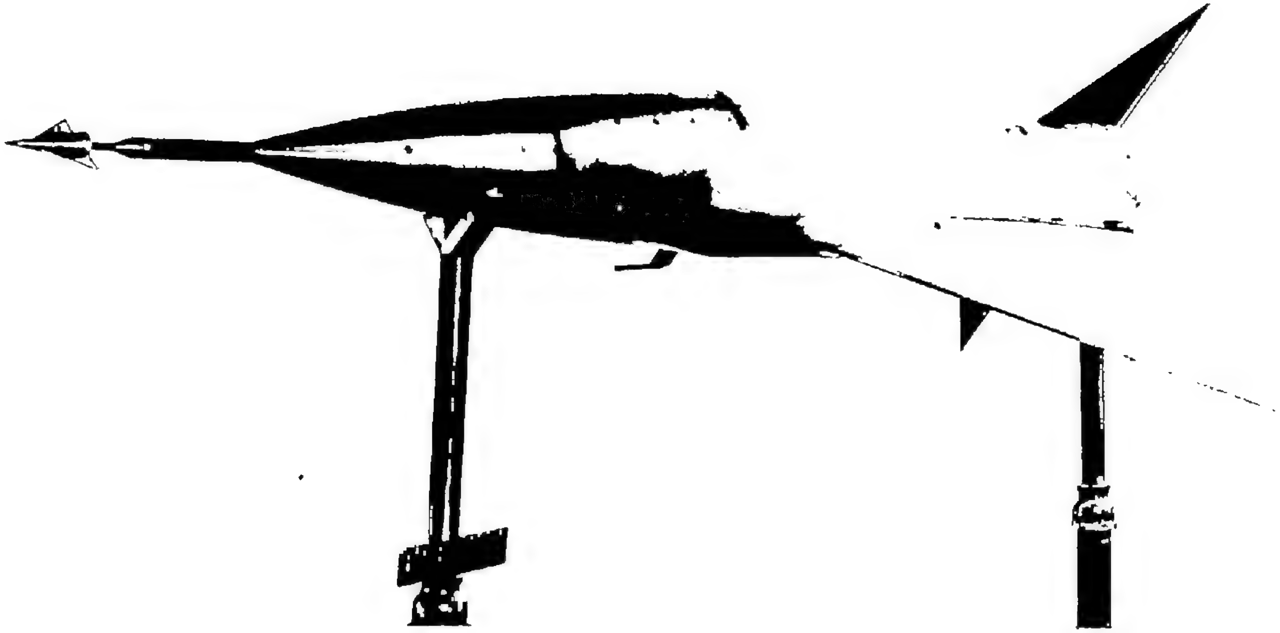

Figure 2.- Photograph of one of the models.

L-78728.1

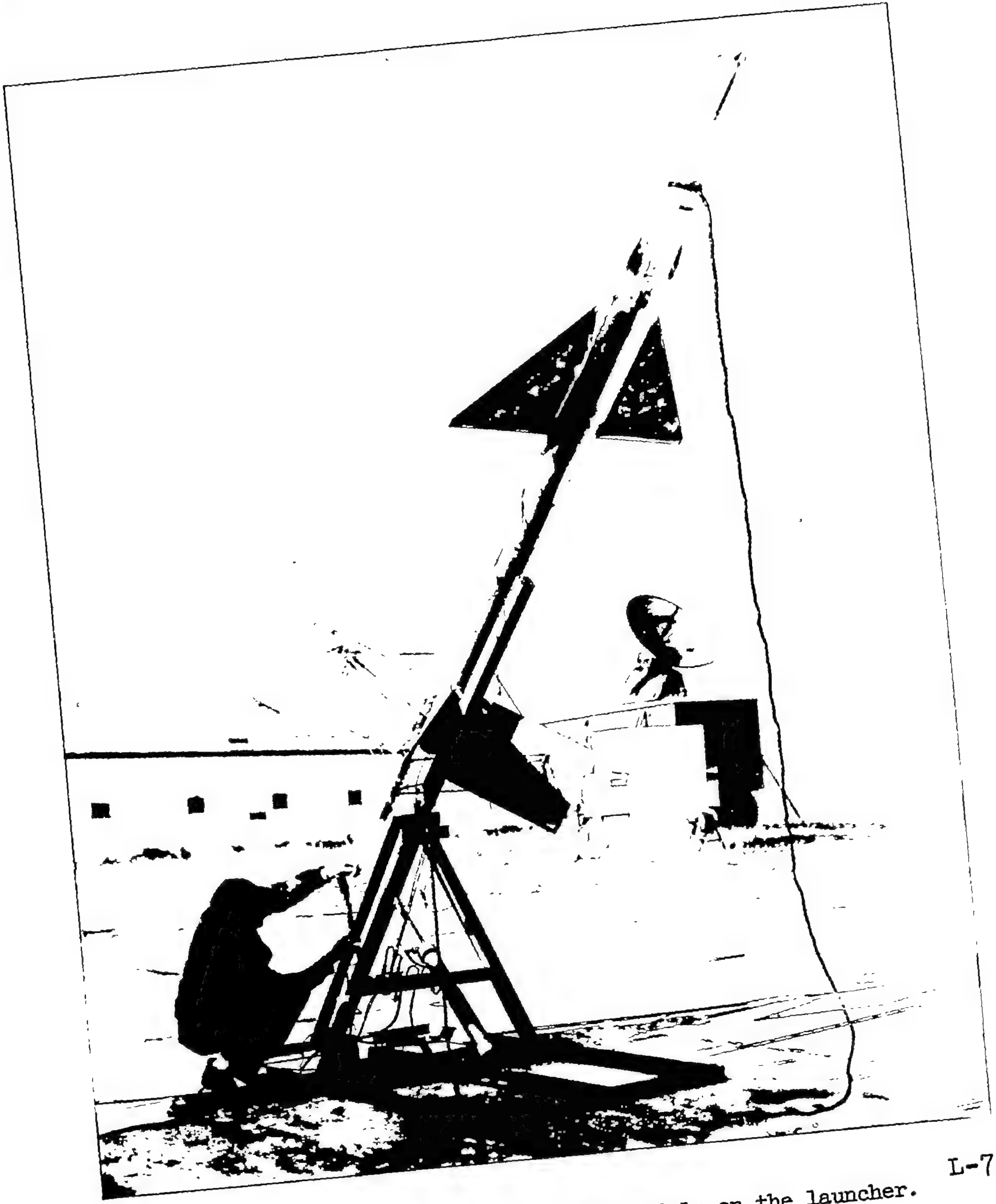

L-78146.1

Figure 3.- Photograph of one of the models on the launcher.

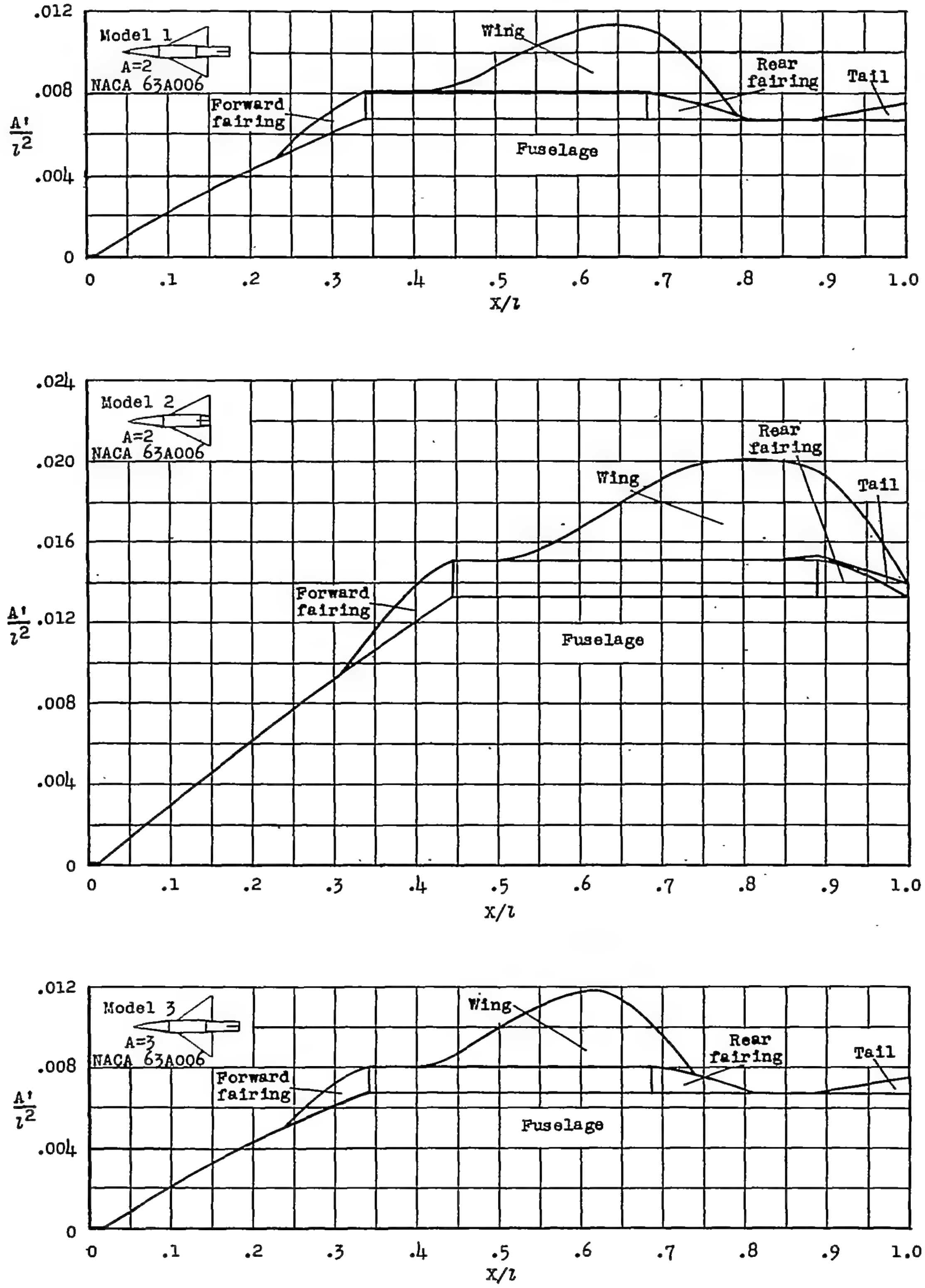

Figure 4.- Longitudinal distribution of cross-sectional area.

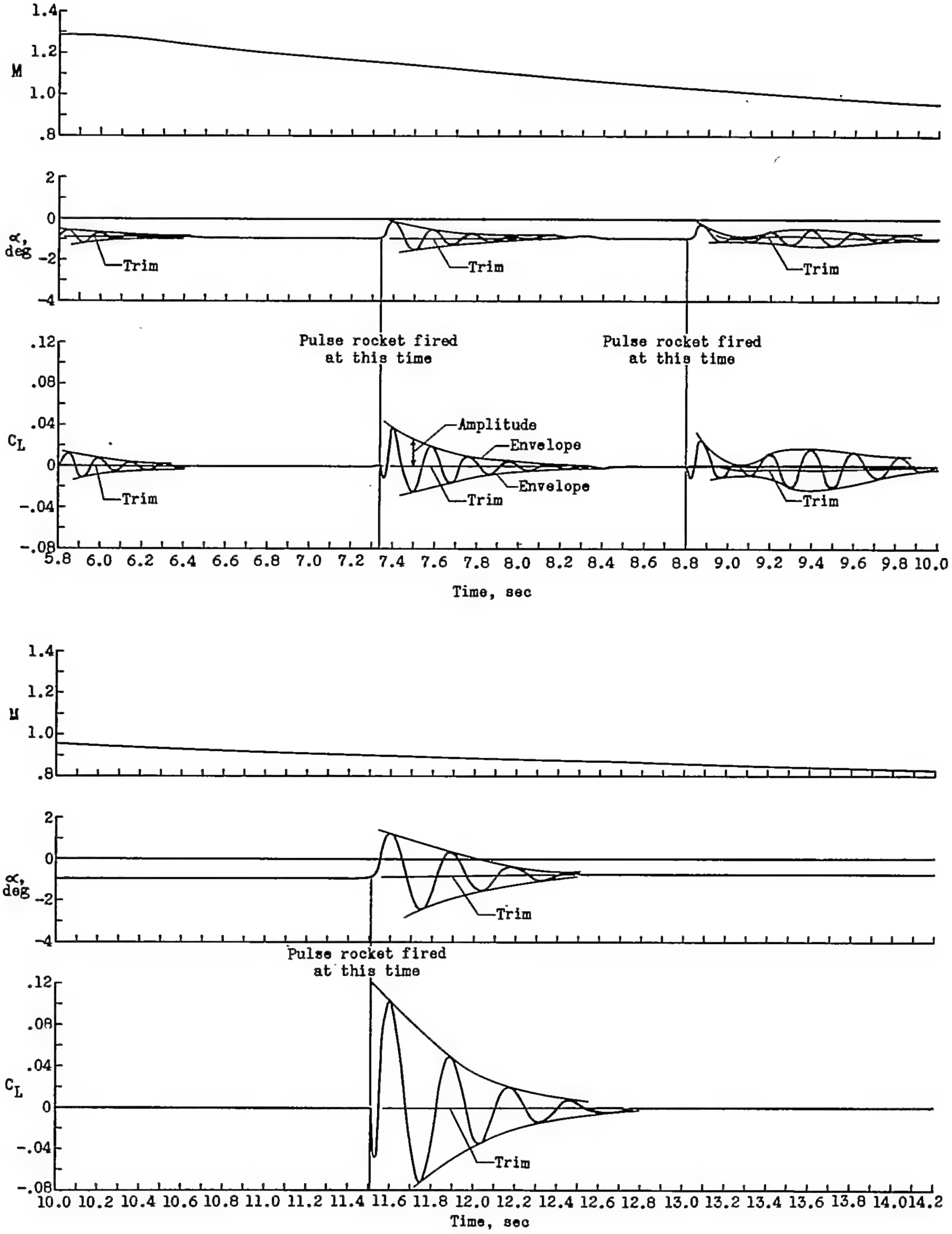

(a) Model 1.

Figure 5.- Time history of flights showing envelopes of the oscillations, trim values, and the time where the pulse rockets were fired.

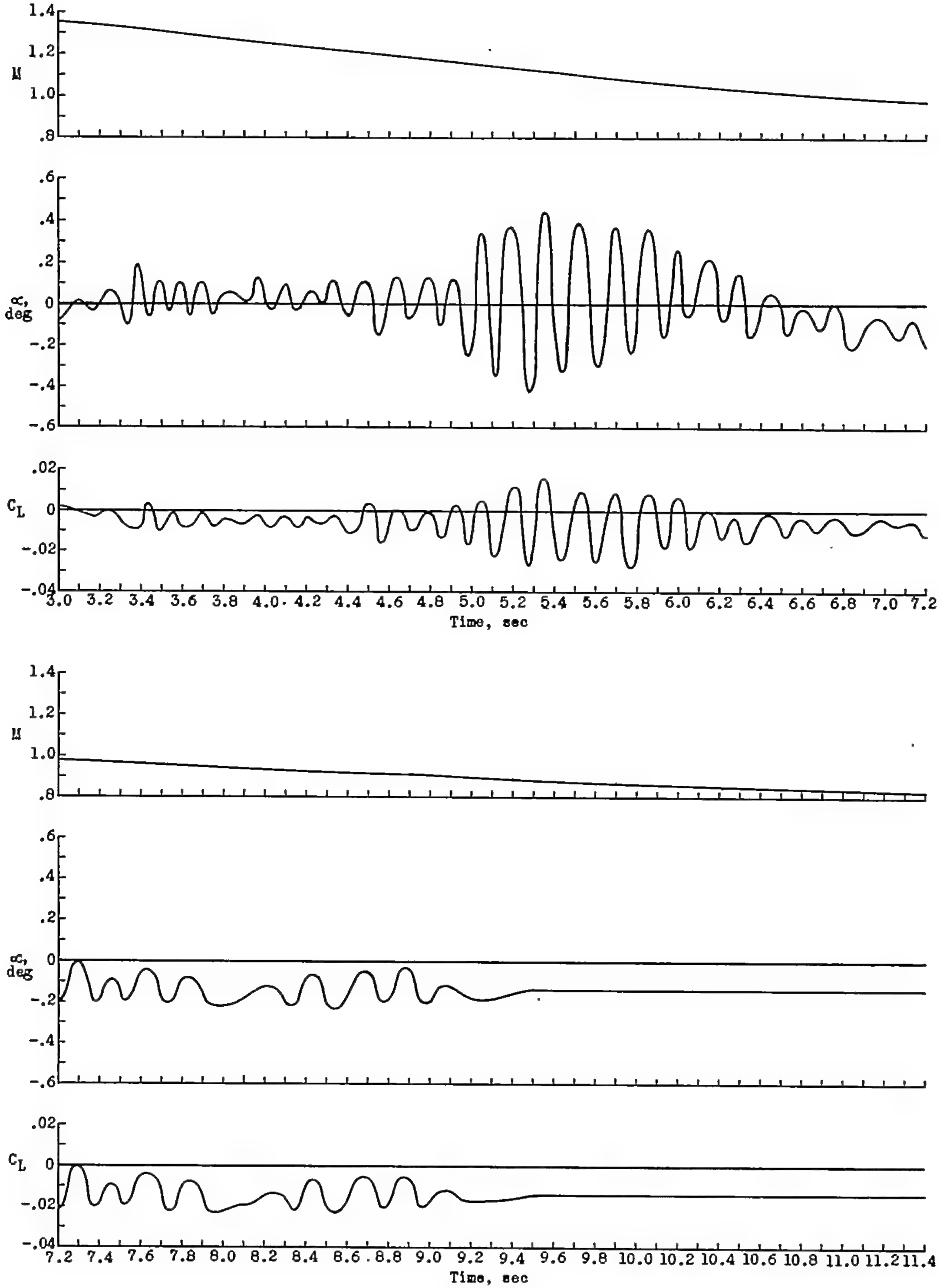

(b) Model 2.

Figure 5.- Continued.

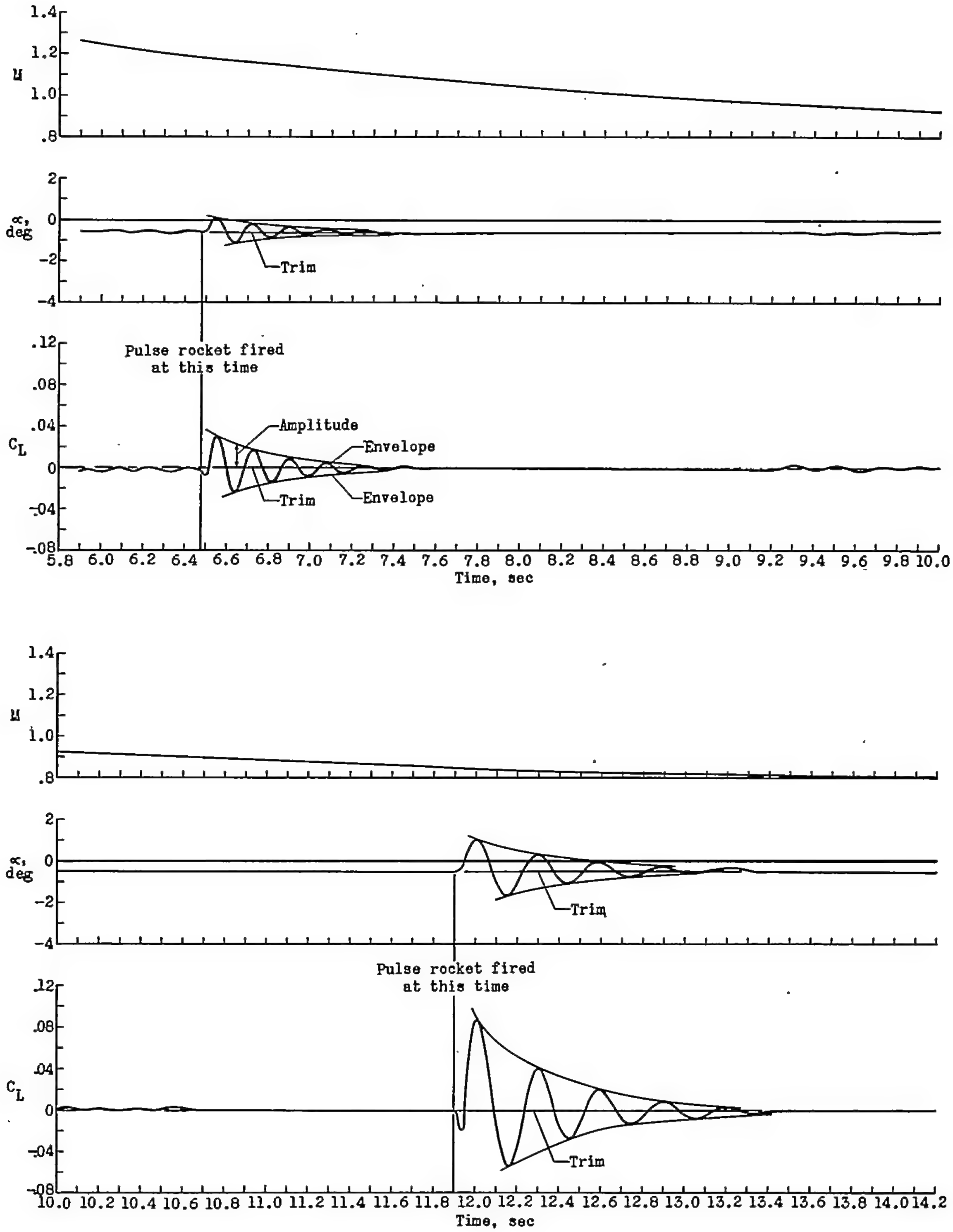

(c) Model 3.

Figure 5.- Concluded.

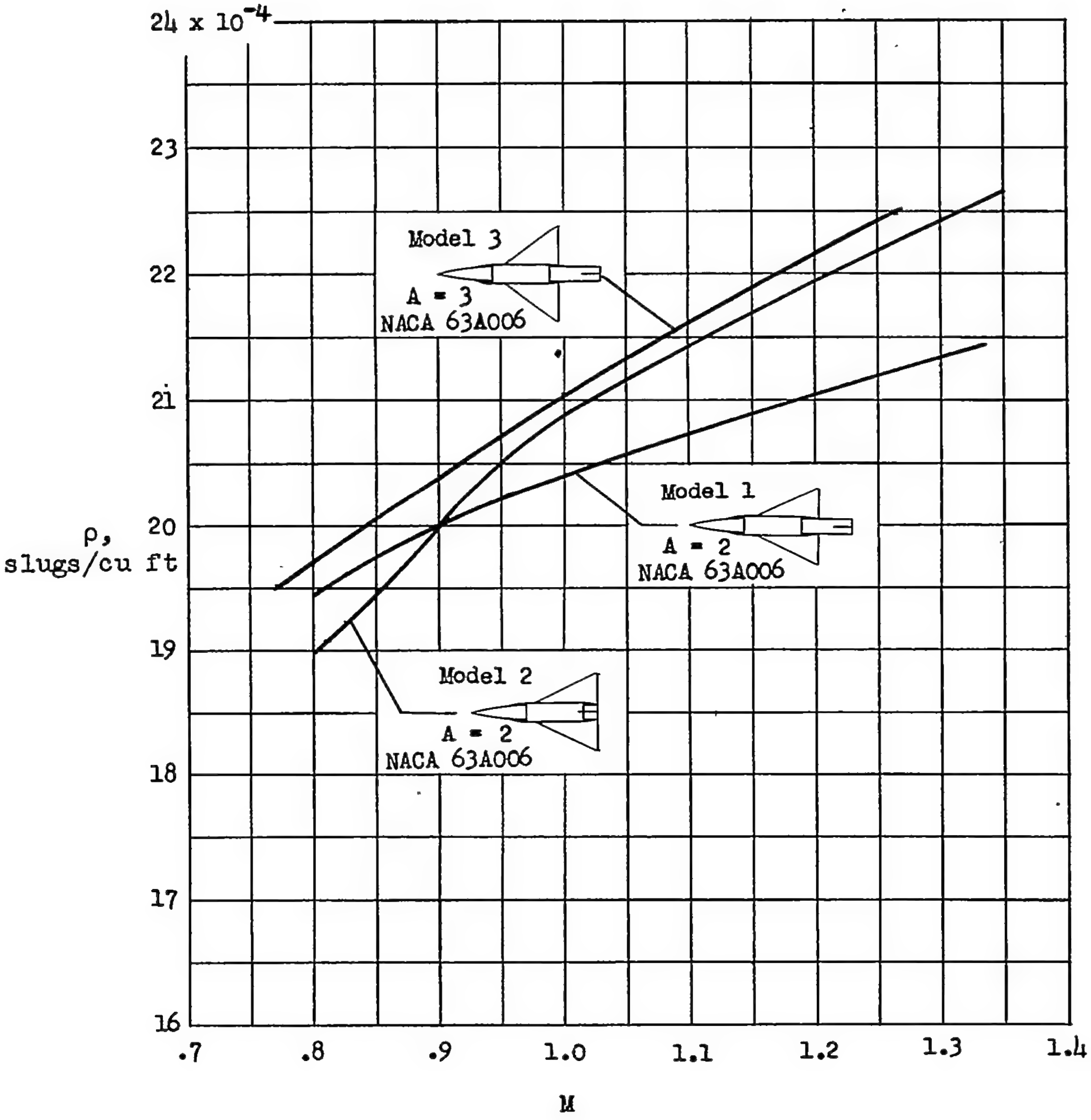

Figure 6.- Variation of air density with Mach number.

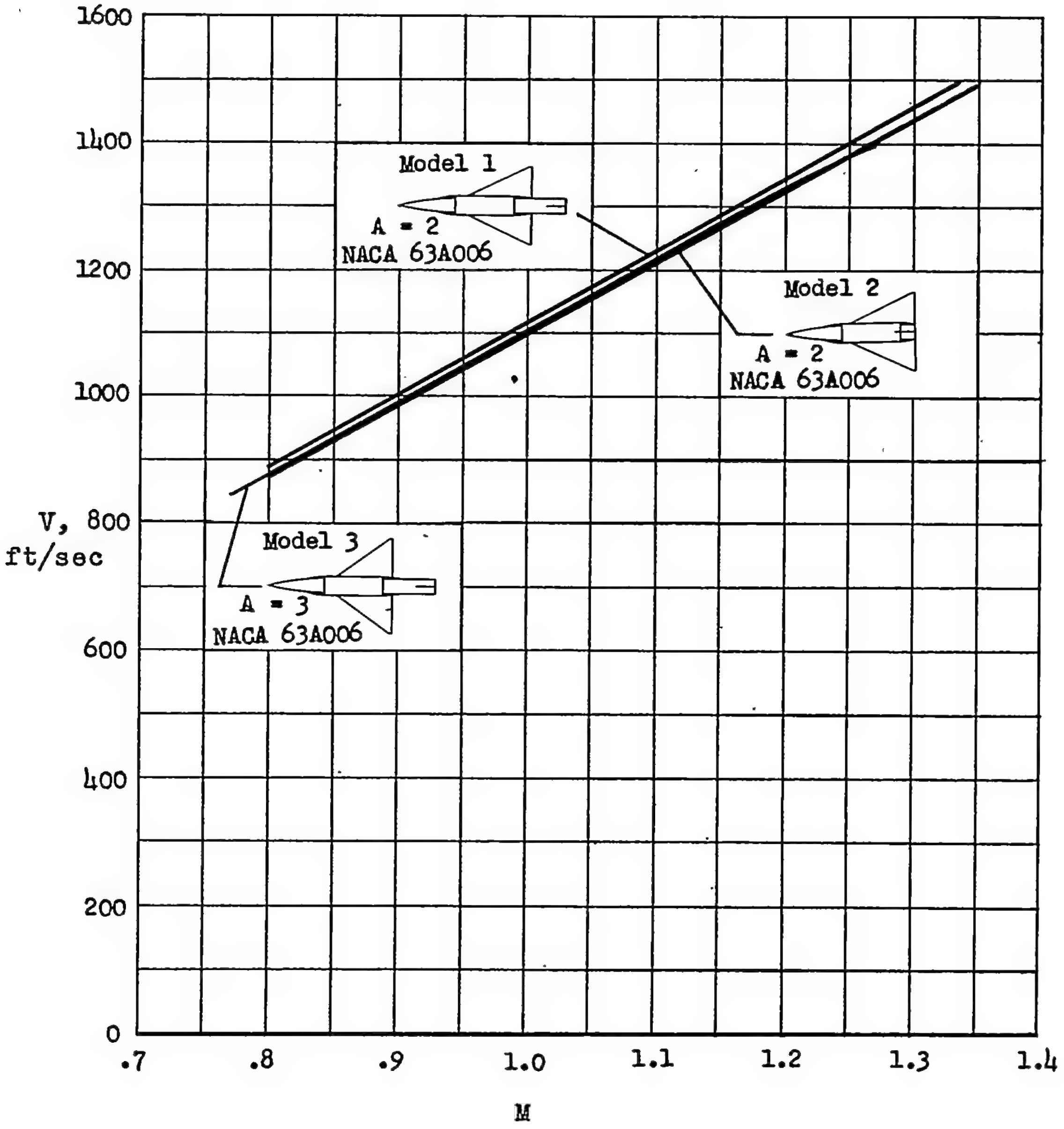

Figure 7.- Variation of velocity with Mach number.

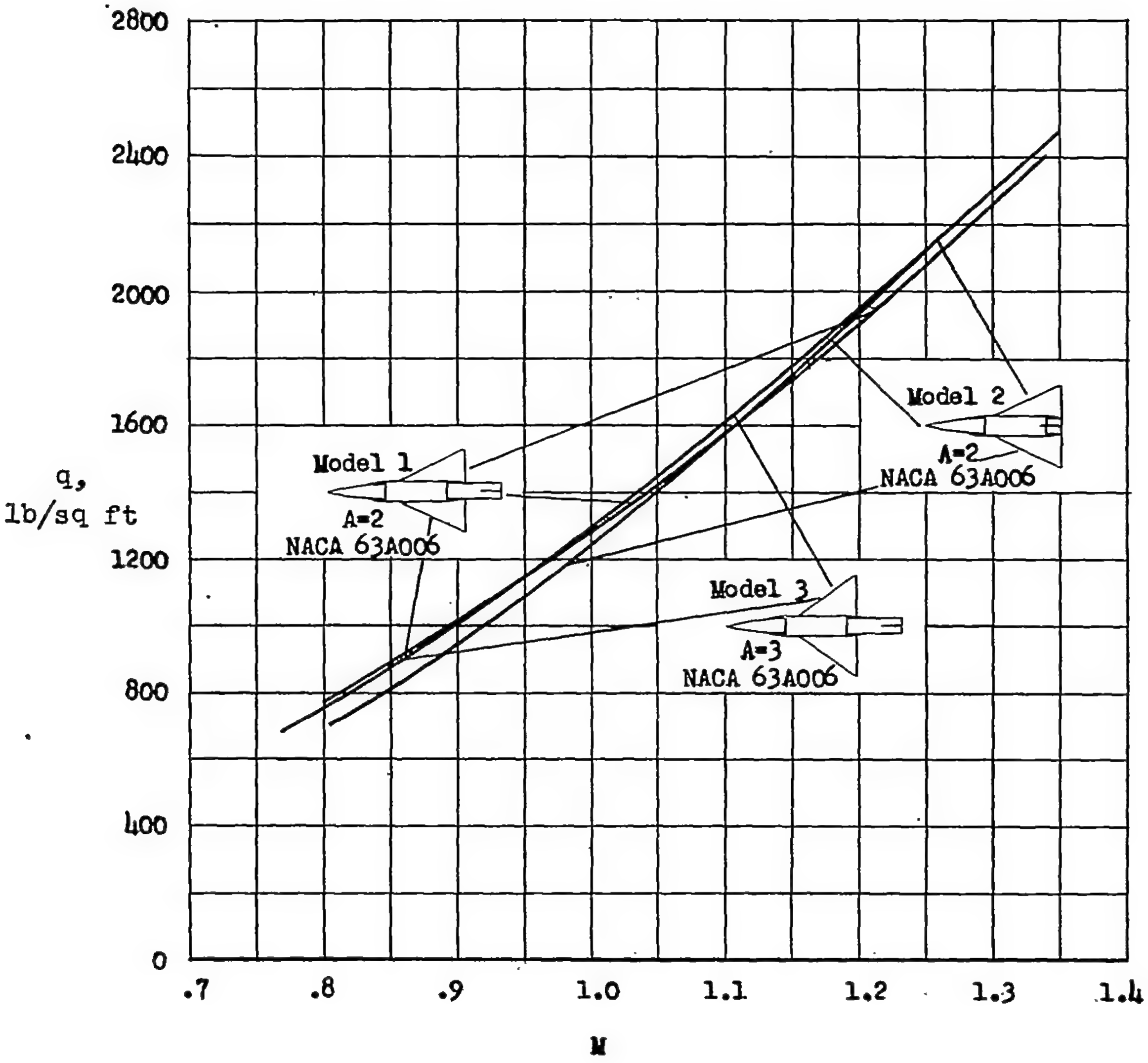

Figure 8.- Variation of dynamic pressure with Mach number.

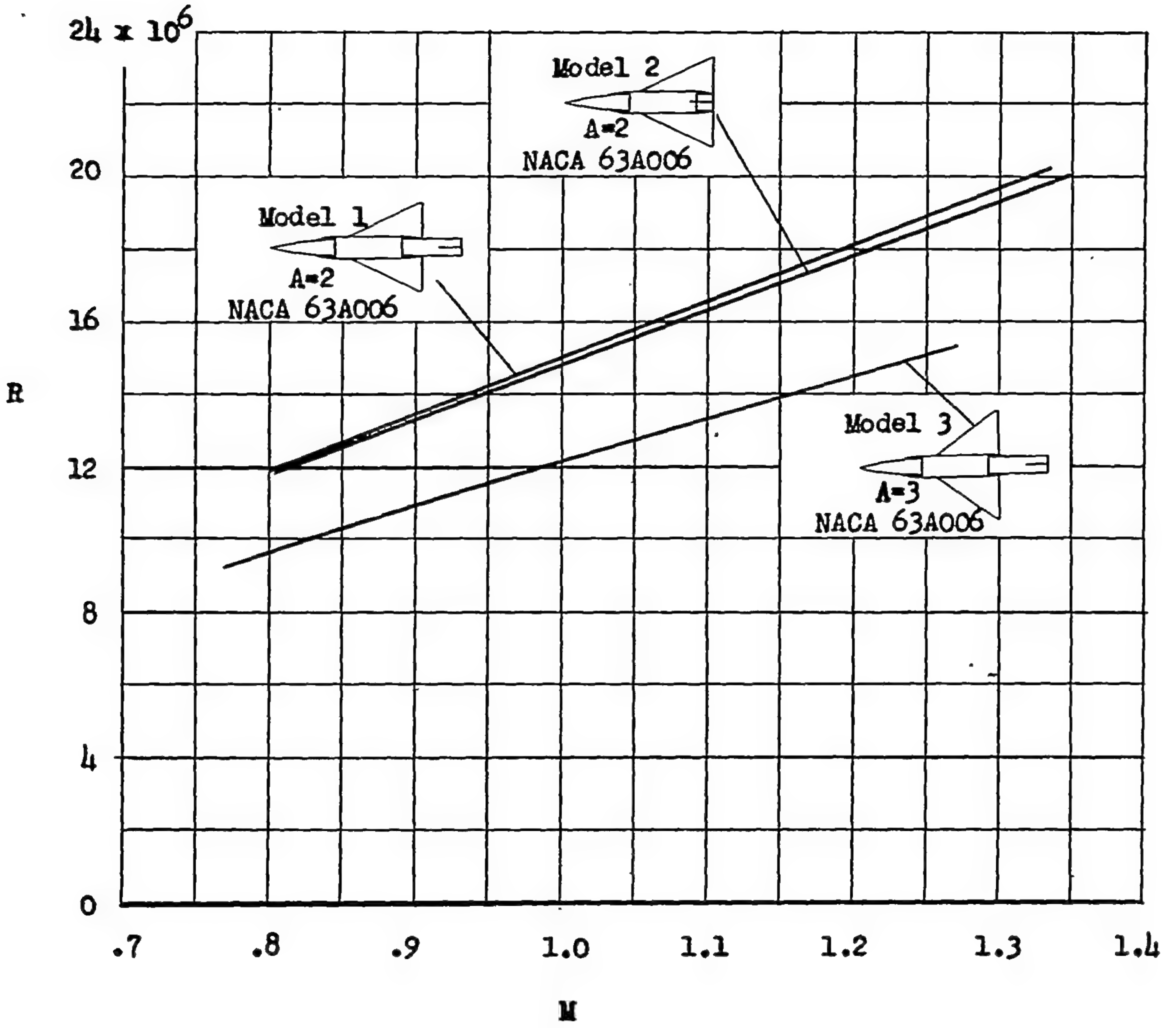

Figure 9.- Scale of tests based on respective mean aerodynamic chord.

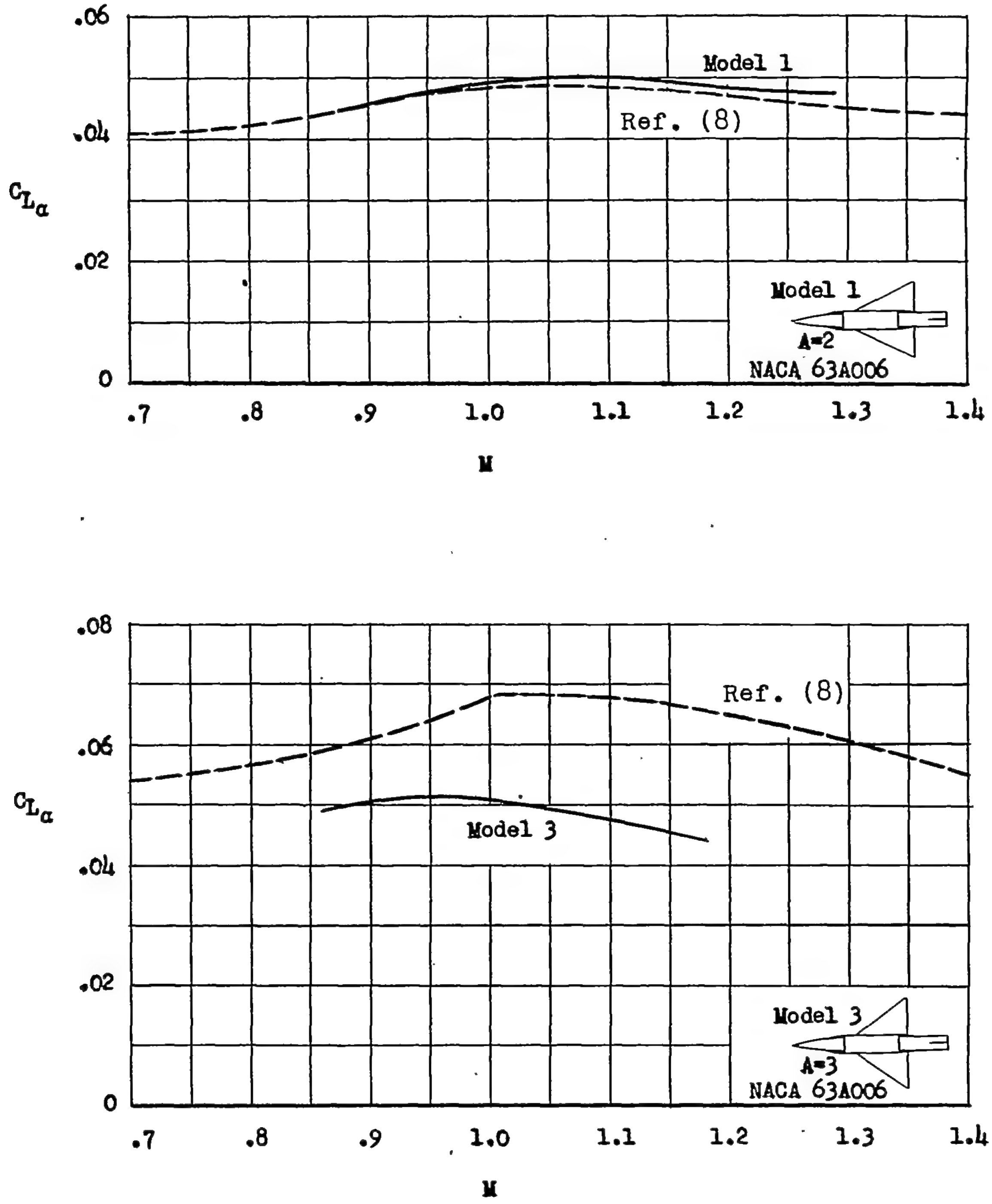

Figure 10.- Comparison of the slope of the lift curve.

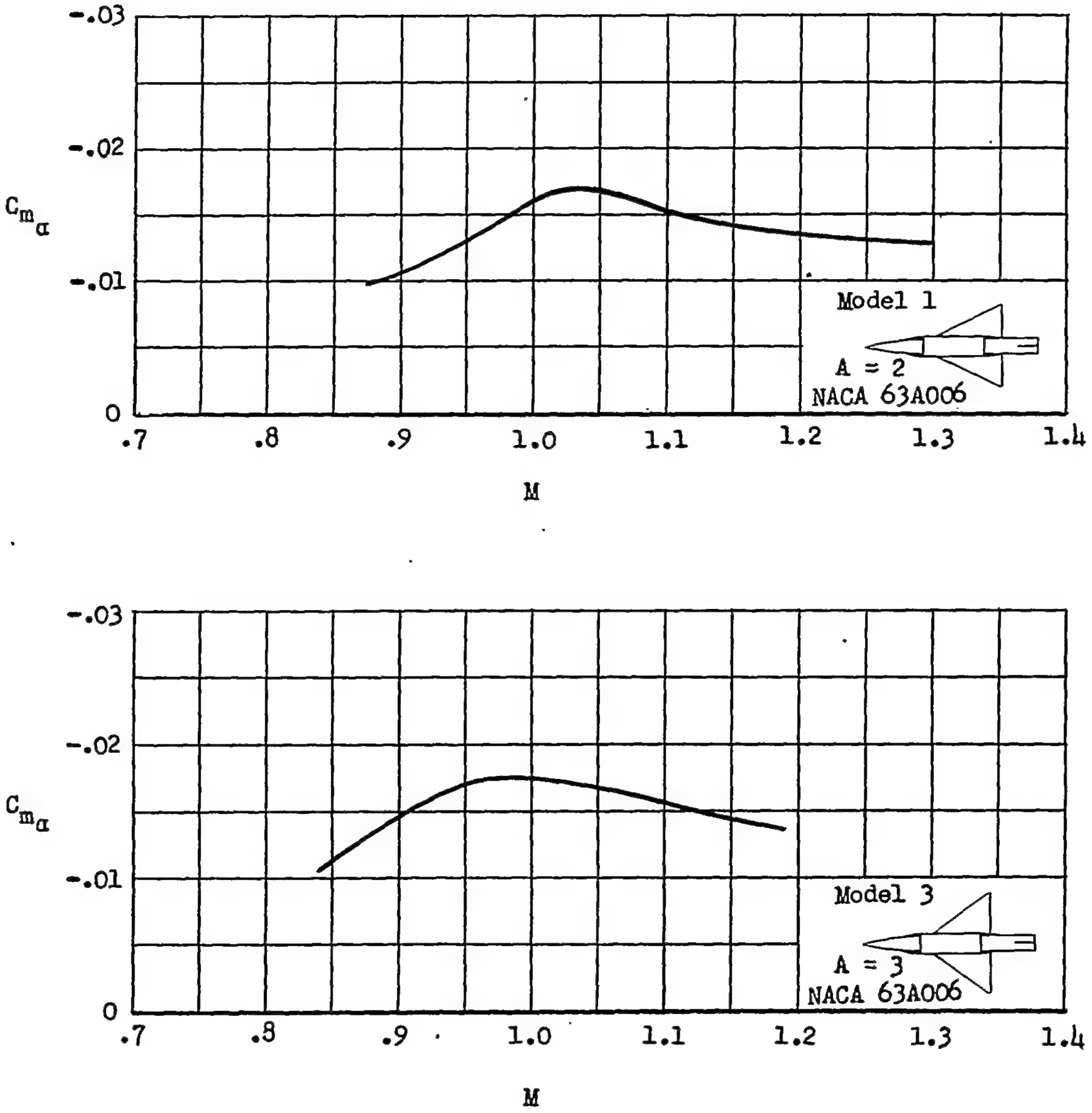

Figure 11.- Variation of the slope of the pitching-moment curve with Mach number.

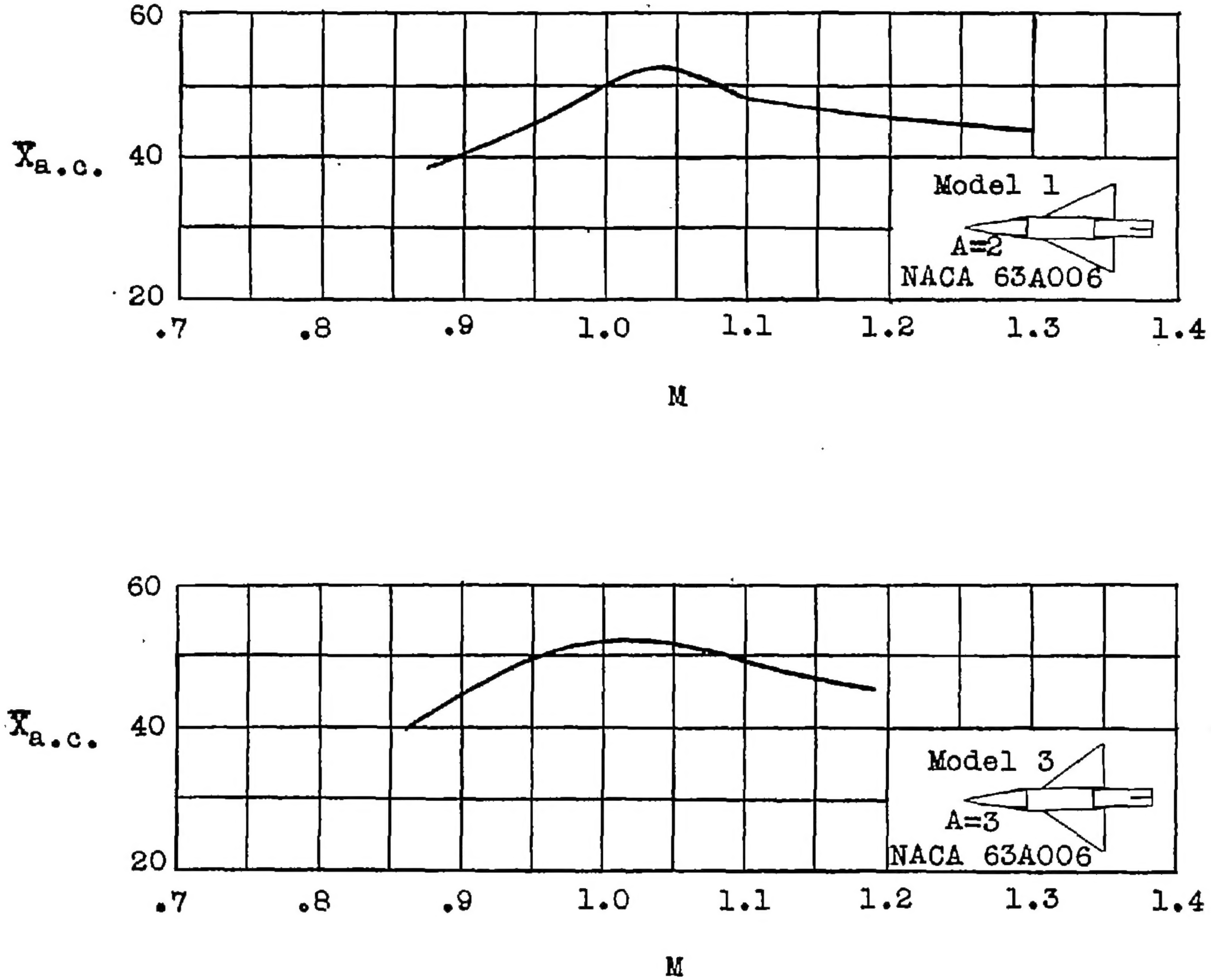

Figure 12.- Variation of the aerodynamic-center location with Mach number.

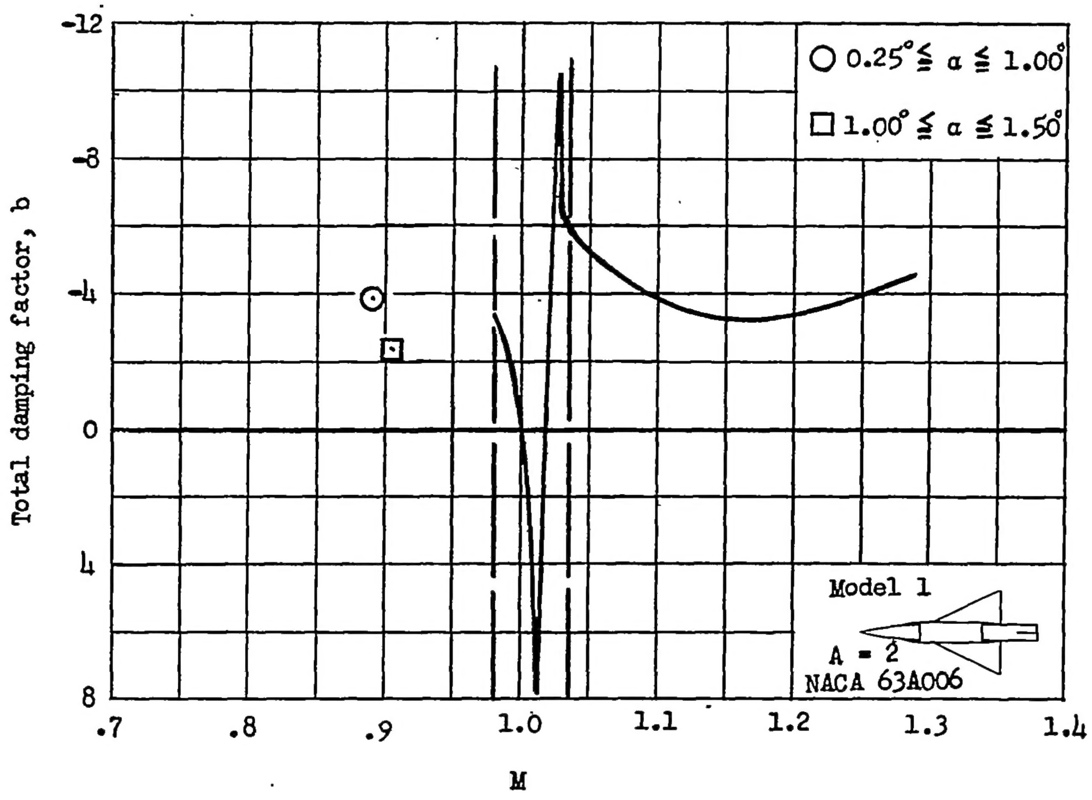

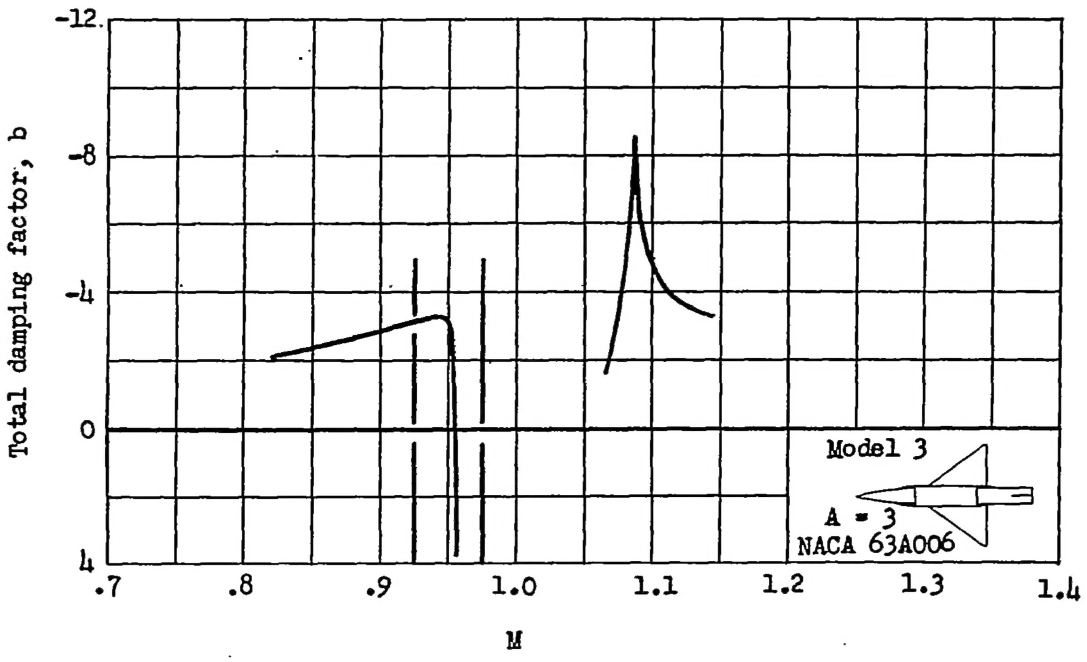

Figure 13.- Variation of the total damping factor with Mach number. (The vertical long-dash lines represent region of limited data.)

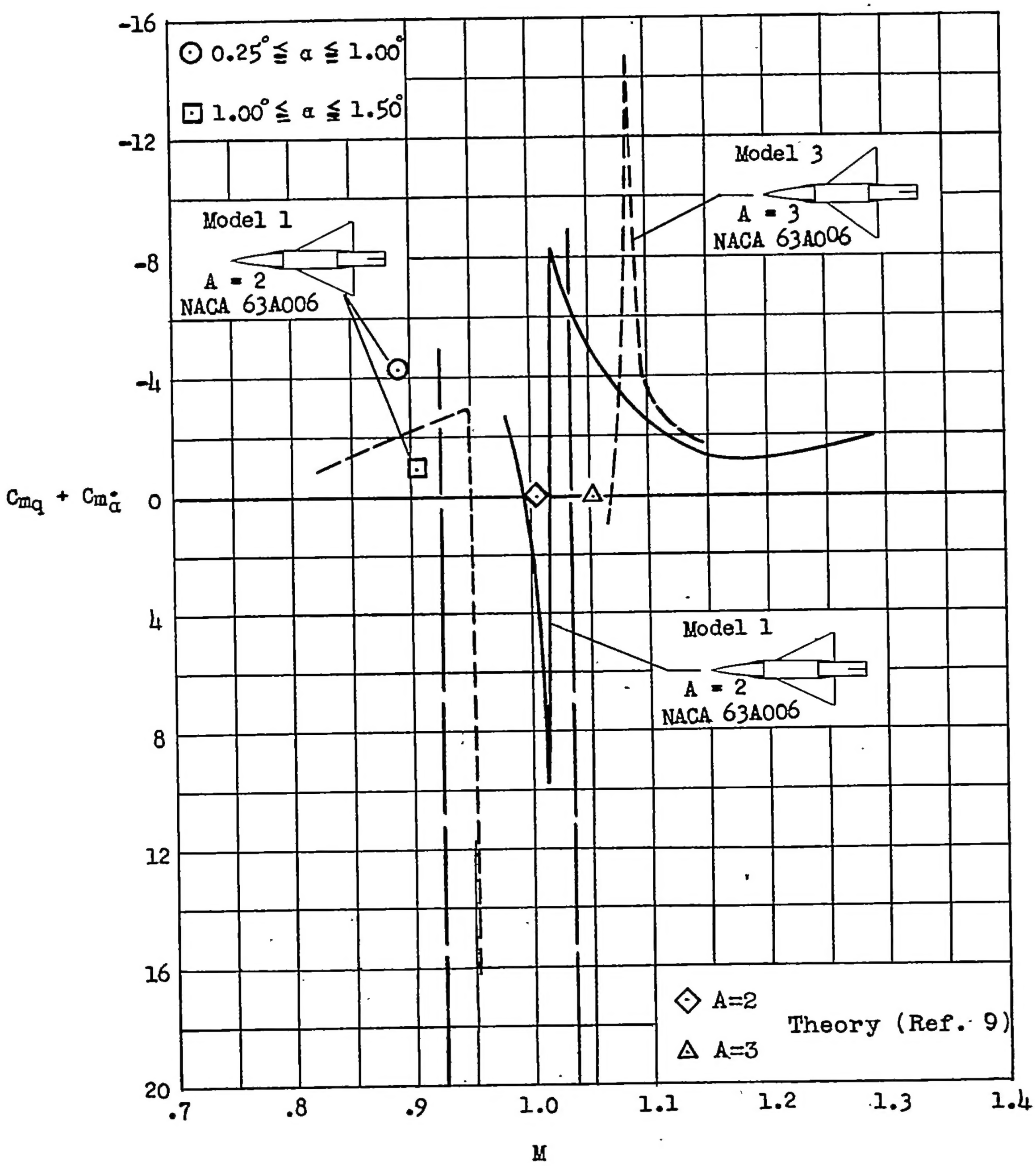

Figure 14.- Variation of the rotational damping-in-pitch derivatives with Mach number. (The vertical long-dash lines represent region of limited data.)

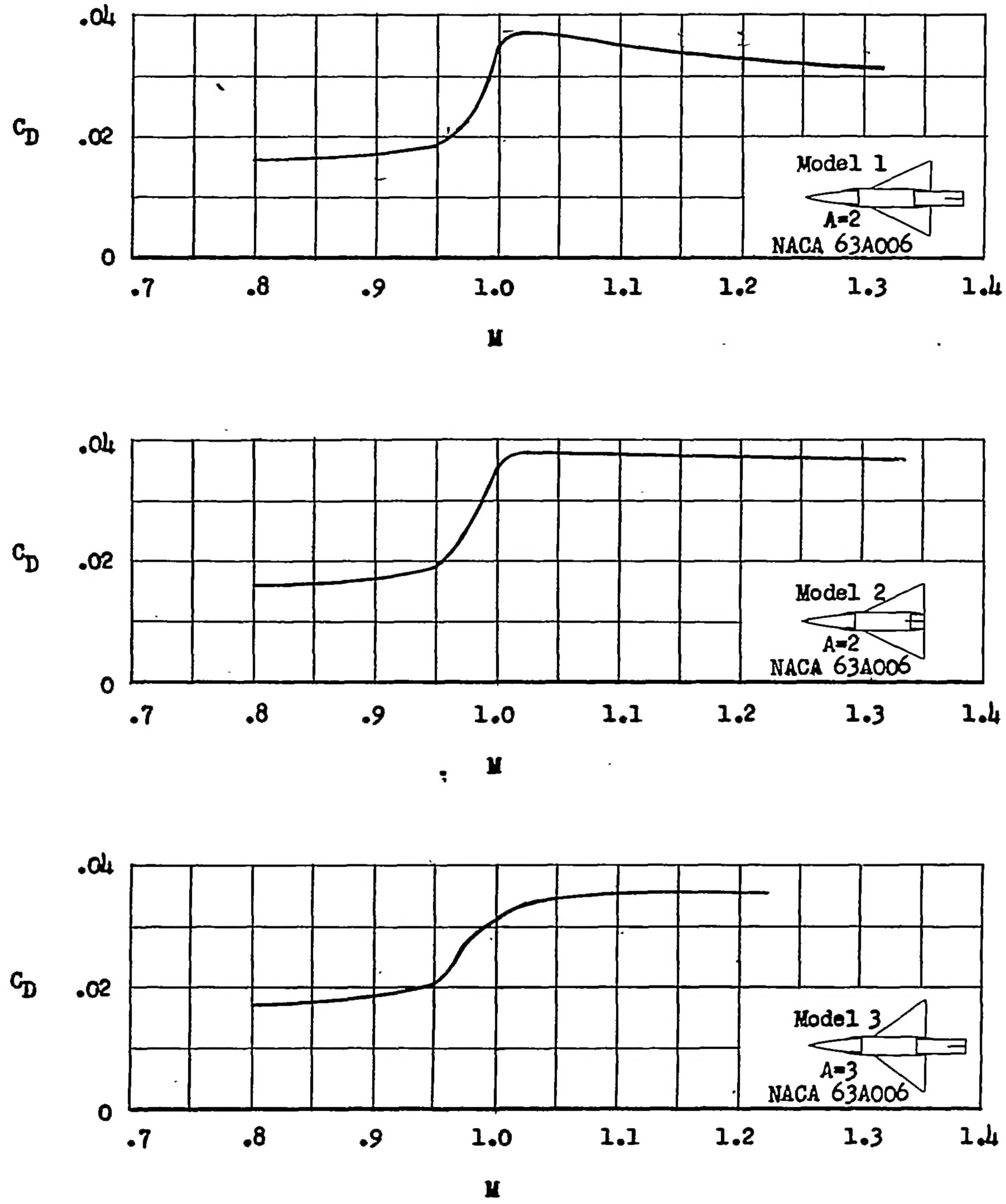

Figure 15.- Variation of the drag coefficient with Mach number.

[redacted]